Journal of Bone Oncology 19 (2019) 100257

Contents lists available at ScienceDirect

Journal of Bone Oncology

journal homepage: www.elsevier.com/locate/jbo

Research Paper

Mouse model recapitulates the phenotypic heterogeneity of human adult T-cell leukemia/lymphoma in bone

Nicole A. Kohart[a], Said M. Elshafae[a,d,e], Wachirapan Supsahvad[a,f], Aylin Alasonyalilar-Demirer[a,g], Amanda R. Panfil[a], Xiang Jingyu[b], Wessel P. Dirksen[a], Deborah J. Veis[b], Patrick L. Green[a], Katherine N. Weilbaecher[b], Thomas J. Rosol[a,c,*]

[a] Department of Veterinary Biosciences, College of Veterinary Medicine, The Ohio State University, Columbus, OH 43210, USA
[b] Department of Medicine, Division of Oncology, Washington University School of Medicine, St. Louis, MO 63110, USA
[c] Department of Biomedical Sciences, Heritage College of Osteopathic Medicine, Ohio University, 225 Irvine Hall, Athens, OH 45701, USA
[d] Department of Radiology, College of Medicine, The Ohio State University, Columbus, OH 43210, USA
[e] Department of Pathology, Faculty of Veterinary Medicine, Benha University, Kalyubia 3736, Egypt
[f] Department of Pathology, Faculty of Veterinary Medicine, Kasetsart University, Bangkok, Thailand
[g] Department of Pathology, Faculty of Veterinary Medicine, Bursa Uludag University, 16059 Bursa, Turkey

ARTICLE INFO

Keywords:
HTLV-1
Lymphoma
Mouse model
Metastasis
Bone resorption

ABSTRACT

Adult T-cell leukemia/lymphoma has a unique relationship to bone including latency in the marrow, and development of bone invasion, osteolytic tumors and humoral hypercalcemia of malignancy. To study these conditions, we established and characterized a novel mouse model of ATL bone metastasis. Patient-derived ATL cell lines including three that do not express HTLV-1 oncoprotein Tax (ATL-ED, RV-ATL, TL-Om1), an *in vitro* transformed human T-cell line with high Tax expression (HT-1RV), and an HTLV-1 negative T-cell lymphoma (Jurkat) were injected intratibially into NSG mice, and were capable of proliferating and modifying the bone microenvironment. Radiography, μCT, histopathology, immunohistochemistry, plasma calcium concentrations, and qRT-PCR for several tumor-bone signaling mRNAs were performed. Luciferase-positive ATL-ED bone tumors allowed for *in vivo* imaging and visualization of bone tumor growth and metastasis over time. ATL-ED and HT-1RV cells caused mixed osteolytic/osteoblastic bone tumors, TL-Om1 cells exhibited minimal bone involvement and aggressive local invasion into the adjacent soft tissues, Jurkat cells proliferated within bone marrow and induced minimal bone cell response, and RV-ATL cells caused marked osteolysis. This mouse model revealed important mechanisms of human ATL bone neoplasms and will be useful to investigate biological interactions, potential therapeutic targets, and new bone-targeted agents for the prevention of ATL metastases to bone.

1. Introduction

Adult T-cell leukemia/lymphoma (ATL) is an aggressive hematological malignancy of $CD4^+$ T-lymphocytes that develops in 2–5% of human T-cell leukemia virus type 1 (HTLV-1)-infected individuals [1–3]. ATL develops after a 20–40 year latency and is associated with a poor prognosis. About half of the acute ATL patients develop humoral hypercalcemia of malignancy (HHM) due to increased tumor-induced osteoclast activity and pathologic bone resorption [4–8]. Transcriptional activator from the X region (Tax) and HTLV-1 basic zipper protein (Hbz) are critical regulatory genes in HTLV-I. Tax is a viral oncogene that regulates the transcriptional activity of the virus, while HBZ antagonizes Tax and promotes proliferation of infected cells [9]. In patients with ATL, especially those with the acute and lymphoma subtypes, serum levels of tumor-produced, bone acting factors, such as parathyroid hormone-related protein (PTHrP), C—C motif chemokine

Abbreviations: HTLV-1, Human T-cell leukemia virus type 1; ATL, adult T-cell leukemia/lymphoma; HHM, humoral hypercalcemia of malignancy; Tax, transcriptional activator from the X region; Hbz, HTLV-1 basic zipper protein; NOD, non-obese diabetic; SCID, CB17-Prkdcscid; NSG, NOD-scid IL2Rgammanull; NK, natural killer; μCT, micro-computed tomography; qRT-PCR, quantitative real-time polymerase chain reaction

* Corresponding author at: Department of Biomedical Sciences, Heritage College of Osteopathic Medicine, Ohio University, 225 Irvine Hall, Athens, OH 45701, USA.

E-mail addresses: Said.Elshafae@osumc.edu (S.M. Elshafae), panfil.6@osu.edu (A.R. Panfil), xiangjingyu@wustl.edu (J. Xiang), dirksen.8@osu.edu (W.P. Dirksen), dveis@wustl.edu (D.J. Veis), green.466@osu.edu (P.L. Green), kweilbae@wustl.edu (K.N. Weilbaecher), rosolt@ohio.edu, rosol.1@osu.edu (T.J. Rosol).

https://doi.org/10.1016/j.jbo.2019.100257
Received 26 April 2019; Received in revised form 16 August 2019; Accepted 19 August 2019
Available online 20 August 2019

ligand 3 (CCL3/MIP-1α), interleukin-1 (IL-1), interleukin-6 (IL-6) and receptor activator of nuclear factor kappa-B ligand (RANKL) are increased [8,10,11]. The expression profile of osteolytic signals is variable between ATL patients with bone lesions resulting in a spectrum of tumor-bone phenotypes [10–13]. The enhanced pathologic bone resorption in ATL patients is primarily controlled through humoral or endocrine-mediated mechanisms. However, several case reports have identified primary ATL bone tumors that also express osteoclast stimulatory factors, indicating a paracrine role for ATL factors in bone as well [14–16]. Few studies have focused on the mechanisms by which humoral or paracrine tumor-growth factors and cytokines from ATL cells induce osteolysis and promote tumor progression.

The bone microenvironment is complex and consists of cells that foster a fertile site for primary and metastatic bone tumors. These cells include hematopoietic precursors, bone marrow stromal cells (BMSC), endothelial cells, osteocytes, osteoblasts (OB), and osteoclasts (OC), all of which may be influenced by tumor cells to induce bone into a protumorigenic microenvironment. Once tumor cells seed within the bone marrow, tumor-derived factors (such as PTHRP) upregulate RANKL on OBs which enhances RANK-RANKL signaling, OC differentiation and activation, and subsequent bone resorption. This mechanism, among others, disrupts the normal bone remodeling process resulting in breakdown of mineralized bone matrix and release of growth factors that promote tumor growth. Bone factors released include transforming growth factor-β (TGF-β), insulin-like growth factors (IGFs), and bone morphogenetic proteins (BMPs), which promote tumor growth and increase the production of bone-acting factors from tumor cells. This phenomenon is known as the 'vicious cycle' [17,18]. Crosstalk between cancer and bone cells has been extensively studied in common bone-metastatic tumors, such as multiple myeloma and breast cancer. However, the interactions between bone and ATL cells remain largely unknown.

Animal models for hematological malignancies that involve bone are necessary for investigation of the molecular and cellular mechanisms of cancer and bone cell interactions and are critical for bench-to-bedside research. The phenotypic diversity of tumor-bone interactions in patients is complex, therefore, multiple animal models will be required to recapitulate unique components of specific tumor types. Xenograft mouse models of tumors in bone have utilized several approaches, including direct inoculation into bone or spontaneous osseous spread after intracardiac injection. In this study, we have employed direct intratibial injection to model tumor-bone interactions without considering aspects of metastatic spread to bone, which are less relevant for hematologic malignancies that have ready access to the bone as they circulate. The five cell lines characterized in this study differ in their expression of the HTLV-1 oncogenes Tax and Hbz and demonstrate significant phenotypic diversity. Thus, they provide a valuable platform to explore tumor-bone signaling pathways and to elucidate novel mechanisms by which ATL influences the bone microenvironment.

2. Materials and methods

2.1. Reagents and cell lines

RV-ATL [19,20], ATL-ED [21,22], and TL-Om1 [23] cell lines were derived from ATL patients. The HT-1RV cell line was developed by superinfection of RV-ATL cells with HTLV-1 to create a cell line with high-Tax expression [24]. The HT-1RV cell line was maintained in Iscove's medium (Corning, Manassas, VA, USA) supplemented with 10% FBS, 2 mM glutamine, 100 U/mL penicillin, and 100 μg/mL streptomycin. HEK293T cells were maintained in DMEM medium (Invitrogen) supplemented with 10% FBS, 2 mM glutamine, 100 U/mL penicillin, and 100 μg/mL streptomycin. The HTLV-1-negative T cell lymphoma line (Jurkat), and ATL cell lines, ATL-ED, TL-Om1, and RV-ATL, were cultured as previously described [21,25]. Briefly, Jurkat, ATL-ED and TL-Om1 cells were cultured in RPMI 1640 medium supplemented with 10% fetal bovine serum (FBS) L-glutamine (2 mM), penicillin (50 U/ml) and streptomycin (50 mg/ml) (Invitrogen). RV-ATL cells were passaged in non-obese diabetic/ CB17-Prkdcscid (NOD/SCID) mice and briefly cultured in the RPMI 1640 medium above supplemented with 20% FBS prior to tibial injection.

2.2. Animals and inoculation

Male NSG (NOD-scid IL2Rgamma^{null}) mice were acquired from the NSG mouse colony maintained by the Target Validation Shared Resource (TVSR) at the Ohio State University; breeders (Strain #005557) for the colony were received from the Jackson laboratory. Four- to five-week-old male NSG and NOD/SCID (NOD CB17-Prkdc-SCID/J; The Jackson Laboratory, Bar Harbor, ME) mice were housed and treated in accordance with the University Laboratory Animal Resources guidelines, and experimental protocols were approved by the Institutional Laboratory Animal Care and Use Committee. Intratibial injections were performed to recapitulate bone tumors, as previously described [26]. Briefly, mice were anesthetized in an induction chamber with 3% isoflurane and maintained with 2.5% isoflurane. The right rear limb was shaved with a disposable razor to remove the fur and improve visibility. The distal leg was scrubbed with alcohol-soaked gauze. The leg was held so the knee joint was at a 90° angle and a 27-ga, ½" needle was introduced through the patellar ligament and into the tibial marrow space through the articular cartilage. A Hamilton syringe was used to inject 10 μL containing 200,000–250,000 cells suspended in RPMI 1640 medium (Iscove's medium for the HT-1RV cell line) into the marrow cavity. Successful intratibial injections were verified by: (1) the absence of joint invasion and lameness, (2) the absence of blockage or resistance during the injection, (3) the absence of swelling or bioluminescence in the soft tissue surrounding the tibia after the injection and (4) histopathological analysis at the end of the experiment demonstrating tumor cell invasion through the cortical bone. Mice were euthanized 28–35 days after injection, except for the RV-ATL (38–43 days) and the ATL-ED-luc (20–29 days) mice.

2.3. Measurement of plasma calcium concentrations

Blood was collected using lithium heparin blood collection tubes (Fisher Scientific). Blood was centrifuged and plasma was separated and stored at −20 °C until measurements were performed. Total calcium concentrations in plasma were measured using the QuantiChrom Calcium Assay Kit (BioAssay Systems, Hayward, CA, USA).

2.4. Cytology, histopathology, immunohistochemistry, and enzymatic histochemistry analysis

A complete necropsy was performed on each mouse. Impression smears were made from the cut surfaces of the tumors, stained with Modified Wright–Giemsa, and evaluated cytologically. Tibias and femurs were removed, defleshed, and fixed in 10% neutral-buffered formalin (NBF) for 48 h. Tibias and femurs were placed in 70% ethanol for 24 h for μCT and faxitron imaging. After images were collected, tibias and femurs were decalcified with mild Decalcifier (formaldehyde, methanol and formic acid) (Leica Biosystems, Buffalo Grove, IL), embedded in paraffin, sectioned and stained with H&E for histopathologic evaluation. Femurs were processed similarly. Sections of liver, lung, kidney, adrenal gland, spleen, and lymph node were fixed in 10% NBF for 48 h, embedded in paraffin, sectioned, and stained with H&E for histopathologic (micrometastasis) evaluation. Additional sections were prepared for immunohistochemistry and enzymatic histochemistry. Immunohistochemistry for human leukocyte antigen (1:100; Abcam, Cambridge, MA, USA) was performed on paraffin-cut sections. Enzymatic histochemistry for tartrate-resistant acid phosphatase (TRAP) was performed to identify osteoclasts (Sigma-Aldrich, St. Louis,

MO, USA) as previously described [27].

2.5. Radiographic imaging

Formalin-fixed tibias and femurs were soaked in ethanol for 48 h in preparation for radiographic imaging. Tibias and femurs were placed centrally on a Faxitron laboratory radiography system LX-60 (Faxitron X-ray Corp., Wheeling, IL) imaging platform and high-resolution radiographs were taken (for 2–6 s at 22–28 kV). The degree of radiolucency was used as a surrogate for bone loss and was quantified using Bioquant Osteo 2010 software (Version 10.3.60MR). Radiograph DICOM images were uploaded, the perimeter of each tibia was outlined and areas were measured. Areas of radiolucency were then outlined and measured for each tibia. Percent of tumor-associated bone loss was calculated by dividing the area of radiolucency (bone loss) over the measured total tibial area for each sample.

2.6. Microcomputed tomography (μCT)

Tibias were placed in a 17-mm holder and imaged using microcomputed tomography (μCT) (μCT-40; Scanco Medical). The scanned μCT DICOM images were imported into Inveon Research Workplace 3.0 software (Siemens Medical Solutions USA, Inc.) and a 3D-reconstruction model of the bone was built from 750 2D slices (0.8 mm) using standard settings.

2.7. Transduction of ATL-ED cells for bioluminescent imaging

ATL-ED cells were selected for bioluminescent imaging to monitor *in vivo* growth and spread. The pCDH-LTR-1-luc-EF1α-copGFP lentiviral vector was described previously [28]. Briefly, HEK293T cells were transfected with LTR-1-luc lentiviral vector plus DNA vectors encoding HIV Gag/Pol and VSV-G in 10-cm dishes using Lipofectamine®2000 reagent according to manufacturer's instructions. Media containing the lentiviral particles were collected 72 h later and filtered through 0.45-μm-pore-size filters (Fisher Scientific). Lentiviral particles were then concentrated using ultracentrifugation in a Sorvall SW-41 swinging bucket rotor at 90,000 x g for 1.5 h at 4 °C. Target ATL-ED cells were infected with concentrated, unselected LTR-1-luc lentivirus by spinoculation at 2000 × g for 2 h at room temperature.

2.8. Bioluminescent imaging

Bioluminescent imaging of mice was performed using the IVIS 100 *in vivo* imaging system (Caliper Life Sciences) as previously described [26]. Briefly, 0.15 ml of sterile DPBS containing 4.5 mg of D-luciferin (Caliper Life Sciences, Hopkinton, MA) was injected intraperitoneally and imaging was performed 5 min later. Serial images were taken every 2 min until peak photon emission was obtained (approximately 10 min post-injection). Photon signal intensity was quantified using Living-Image software version 2.50 (Caliper Life Sciences). Tumor growth was determined based on change in total flux (photons/s) from day of injection to day of sacrifice.

2.9. RNA extraction, reverse transcription, and real-time qRT-PCR

Immediately after the euthanasia of ATL xenografted mice, tumors were carefully dissected from the tibias, snap frozen in liquid nitrogen and stored at −80 °C until further use. Approximately 20–22 mg of tissue were resuspended in tissue RNA lysis buffer and RNA was isolated using a QuickGene Mini 80 (Autogen). Reverse transcription (cDNA) and quantitative real-time polymerase chain reaction (qRT-PCR) were performed, as previously described [25,26,29]. qRT-PCR was performed using human-specific oligonucleotide primers shown in Table 1. These primers were designed and tested as described previously [26,30]. Relative gene expression was normalized to GAPDH using the ΔΔCt method.

2.10. Statistical analysis

Data were analyzed using Graph Pad Prism 6.0 software (San Diego, CA). Students *t*-test and analysis of variance (ANOVAs) were used for statistical analysis. qRT-PCR values were normalized to *GAPDH* mRNA and were expressed as the fold difference between the groups (mean ± SD). All cell lines were compared against ATL-ED cells in the qRT-PCR graphs using a one-way ANOVA with Dunnett's multiple comparison post hoc test. A p value ≤ 0.05 was considered to be statistically significant. Plasma calcium concentrations were analyzed using a one-way ANOVA. For *in vivo* imaging data of ATL-ED xenografts, the average bioluminescence (photons/s/cm^2) and corresponding standard errors of the mean were determined for each experiment. Quantitative radiographic bone loss determined in ATL xenografts was analyzed statistically with a non-parametric Kruskal–Wallis test.

3. Results

3.1. NSG mice demonstrated superior engraftment of ATL cell lines over NOD/SCID

Two strains of immunosuppressed mice were selected for comparison of tumor cell engraftment in order to optimize tibial injections. Three cell lines were used in this comparison. The RV-ATL and TL-Om1 cell lines (neither express the oncogene Tax) and the HT-1RV cell line (with high Tax mRNA expression) were selected for comparison of tibial engraftment potential between NOD/SCID and NSG mice. The presence or absence of Tax was considered because of its immunogenic potential. Mice were sacrificed at various times (see Section 2) following inoculation, and gross tumor development was recorded. Engraftment of all three cell lines was improved when injected intratibially into the NSG mice compared to the NOD/SCID strain (Fig. 1). In particular, HT-1RV cells went from 0% to 100% engraftment, indicating that Tax was highly immunogenic in the NOD/SCID mice, probably because NOD/SCID mice still have NK cells, while NSG mice do not [31]. None of the NOD/SCID tumor-bearing mice had evidence of metastasis. Distant metastasis was observed in the NSG mice bearing HT-1RV tumors. These results are consistent with previous reports noting the advantage in development of metastasis in xenografted NSG mouse models [32].

3.2. ATL cells engrafted following intratibial inoculation and some developed metastases

Based on the findings above, we determined that the NSG mice were the best strain of mice to use for this study. Thus, NSG mice were also inoculated with ATL-ED and Jurkat cell lines. ATL-ED is another Tax-negative cell line derived from an ATL patient and Jurkat is an HTLV-1-negative T-cell lymphoma cell line that served as a control in our experiments. The percent of tibial engraftment ranged from 62% (TL-Om1; $n = 5/8$, number of engraftments/number of injections), 71% (RV-ATL; $n = 10/14$), 73% (ATL-ED; $n = 25/34$, including ATL-ED-luc injections), 75% (HT-1RV; $n = 6/8$) to 100% for Jurkat ($n = 12/12$) cell lines in the NSG mice. The human origin of the xenografts was confirmed using immunohistochemistry for human-specific leukocyte antigen (Fig. 2). A summary of radiographic and histopathologic characteristics of ATL tumor engraftment is provided in Table 2. Metastasis occurred in mice with the ATL-ED and HT-1RV cell lines. ATL-ED cells formed metastases in both the liver (Fig. 3) and kidney of 3 (out of 5) mice. HT-1RV tumor cells were present in the liver and brain of three and one (out of 4) mice, respectively. Local invasion into the adjacent soft tissues including the gastrocnemius muscle was consistently observed in mice with TL-Om1 and RV-ATL cells. Jurkat tumors crossed the joint space of the knee and grew in the ipsilateral

Table 1
Primers used for qRT-PCR of tumor samples.

Gene name	Forward primer	Reverse primer
glyceraldehyde-3-phosphate dehydrogenase (GAPDH)	GCAAATTCCATGGCACCGTC	AGCATCGCCCCACTTGATTT
parathyroid hormone-related protein (PTHrP)	GTCTCAGCCGCCGCCTCAA	GGAAGAATCGTCGCCGTAAA
parathyroid hormone 1 receptor (PTH1R)	GGCTTCACAGTCTTCGGCT	GAGCACCCGGACGATATTGAT
C-C motif chemokine ligand 3 (CCL3)	CTGCATCACTTGCTGCTGACA	CACTGGCTGCTCGTCTCAAAG
colony stimulating factor 1 (CSF1)	GCAGGAACTCTCTTTGAGGCT	TCTTGACCTTCTCCAGCAACTG
lysophosphatidic acid receptor 1 (LPAR1)	GTAGTTCTGGGGCGTGTTCA	ACCAGCTTGCTGACTGTGTT
tumor necrosis factor (TNF)	CCCTCTGGCCCAGGCAGTCA	CGGCGGTTCAGCCACTGGAG
receptor activator of nuclear factor kappa-B ligand (RANKL)	CCTTTCAAGGAGCTGTGCAA	CATCCACCATCGCTTTCTCT
Osteoprotegerin (OPG)	GGCACCAAAGTAAACGCAGAG	ACGCTGTTTTCACAGAGGTCA
Transcriptional activator from the X region (Tax)	CCGCCGATCCCAAAGAAA	CCGAACATAGTCCCCCAGA
HTLV-1 basic zipper protein (Hbz)	AACTTACCTAGACGGCGGAC	CATGGCACAGGCAAGCATCG.

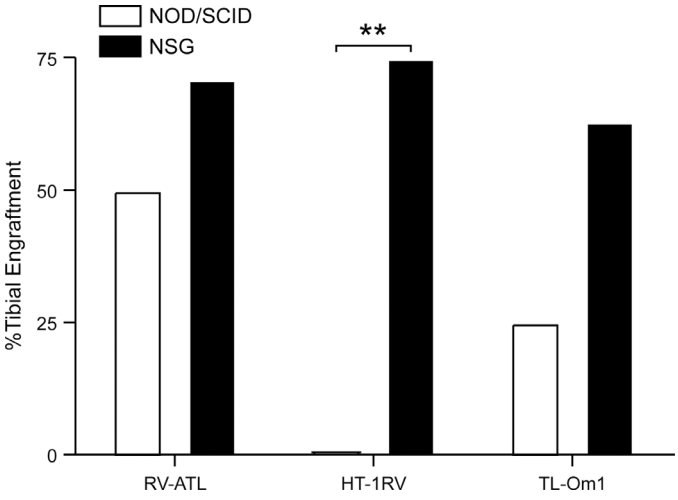

Fig. 1. Tibial tumor engraftment of ATL cell lines in immunosuppressed mice. Improved tumor engraftment in bone following intratibial injection of ATL cell lines, RV-ATL (n = 14 tibias in NSG mice, n = 12 in NOD/SCID mice), HT-1RV (n = 8 tibias for each mouse type), and TL-Om1 (n = 8 tibias for each) in NSG mice compared to NOD/SCID mice.

femoral marrow cavity. This experiment showed that all of the ATL cell lines consistently engraft following intratibial inoculation into NSG mice, while some of them also metastasize occasionally to the liver, kidney and brain.

3.3. Human ATL cells induce osteolytic bone destruction

Patients with ATL often have widespread osteolytic lesions and hypercalcemia [8,33]. We evaluated ATL engrafted mice for osteolysis and bone destruction using X-Ray and μCT scanning. Tibias with ATL-ED tumors showed osteosclerosis (increased radiopacity) within the proximal tibia with multifocal to punctate intralesional, radiolucent areas (Fig. 4(A)), often extending from the proximal tibia to the mid diaphyseal region, and occasionally to the distal diaphysis. In addition, spicules of new bone extending from the proximal to mid-diaphyseal periosteum were present, consistent with periosteal new bone formation (Fig. 4(A)). μCT imaging was consistent with the radiographic findings and demonstrated marked irregular new bone in the marrow cavity as well as on the periosteum (Fig. 6(A)). Similar radiographic and μCT findings were observed in the HT-1RV bone tumors, although the new bone, especially on the periosteum, was not as extensive (Figs. 4(B) and 6(B)). In contrast, tibias with RV-ATL tumors primarily showed bone loss characterized by focal, multifocal, to diffuse areas of radiolucency in the proximal tibia and the diaphysis (Fig. 4(C)). Quantification of bone radiographs showed that the percent of total bone loss per total bone volume was significantly greater in the tibias with RV-ATL tumors compared to the tibias with other tumor types (Fig. 5). TL-Om1 and Jurkat bone tumors demonstrated minimal radiographic evidence of bone pathology, and tibial cortices were smooth and intact. Slight changes in radiopacity and radiolucency were observed (Fig. 4(D)–(E)). Despite minimal evidence of exterior bone pathology of the TL-Om1 and Jurkat bone tumors on longitudinal μCT images (Fig. 6(C)–(D), upper panels), significant differences were observed within the proximal marrow cavity (lower panels). TL-Om1 bones had little trabecular bone compared to Jurkat xenograft tibias, which had moderate amounts of irregular cords of endosteal (intramedullary) new bone extending from the inner cortex into the marrow cavity (Fig. 6(C)–(D)). Blood was collected on the day of sacrifice for measurement of plasma calcium levels. Interestingly, despite marked focal bone resorption and remodeling in several ATL xenografts, plasma calcium concentrations were within the reference range and were similar among all the groups (data not shown), perhaps reflecting the focal nature of bone involvement in this intratibial injection model.

3.4. Enhanced bone remodeling and bone destruction in ATL xenografts

Histopathology was performed on tibial tumors in order to examine the bone remodeling and bone destruction phenotypes more closely. H&E sections of ATL-ED tumor-bearing tibias revealed a large, markedly atypical round cell population diffusely expanding the medullary cavity, invading and destroying the cortical bone, and extending onto the periosteal surface (Fig. 7(A)). The marrow was completely effaced by tumor cells with coagulation necrosis, fibrosis, and marked endosteal new woven bone formation that was characterized by high osteocyte density. Irregular spicules of woven bone were frequently seen irradiating from the surface of cortical bone, consistent with periosteal new bone formation. TRAP staining revealed low to moderate numbers of TRAP-positive osteoclasts distributed along the periosteal new bone surfaces and were rarely seen associated with the remaining trabecular and cortical bone. Cytologic impression smears of ATL-ED tumor cells revealed a large neoplastic round cell population with marked anisocytosis and anisokaryosis. HT-1RV tumor cells effaced the bone marrow cavity expanding longitudinally within the marrow and adjacent femur and laterally through the cortical bone (Fig. 7(B)). In some mice there was invasion into the joint capsule. Marked periosteal new bone formation was present from the proximal tibia to the diaphysis. The marrow had an atypical round to spindle-shaped tumor cell population with regions of coagulation necrosis. Irregular cords of reactive murine stromal cells were present spanning from the cortical and new trabecular bone into the physis.

RV-ATL tumors effaced the marrow cavity, eroded through the bone cortices, and aggressively invaded into the adjacent soft tissues. Marked pathologic bone resorption was present involving cortices and cancellous bone (Fig. 7(C)). Many large TRAP-positive osteoclasts were present along cortical and trabecular bone surfaces. Additionally, osteoclasts were seen detached from trabecular bone surfaces and intercalated among the RV-ATL cells and fibrostromal cells within the medullary cavity (lower panel). The activity and number of osteoclasts

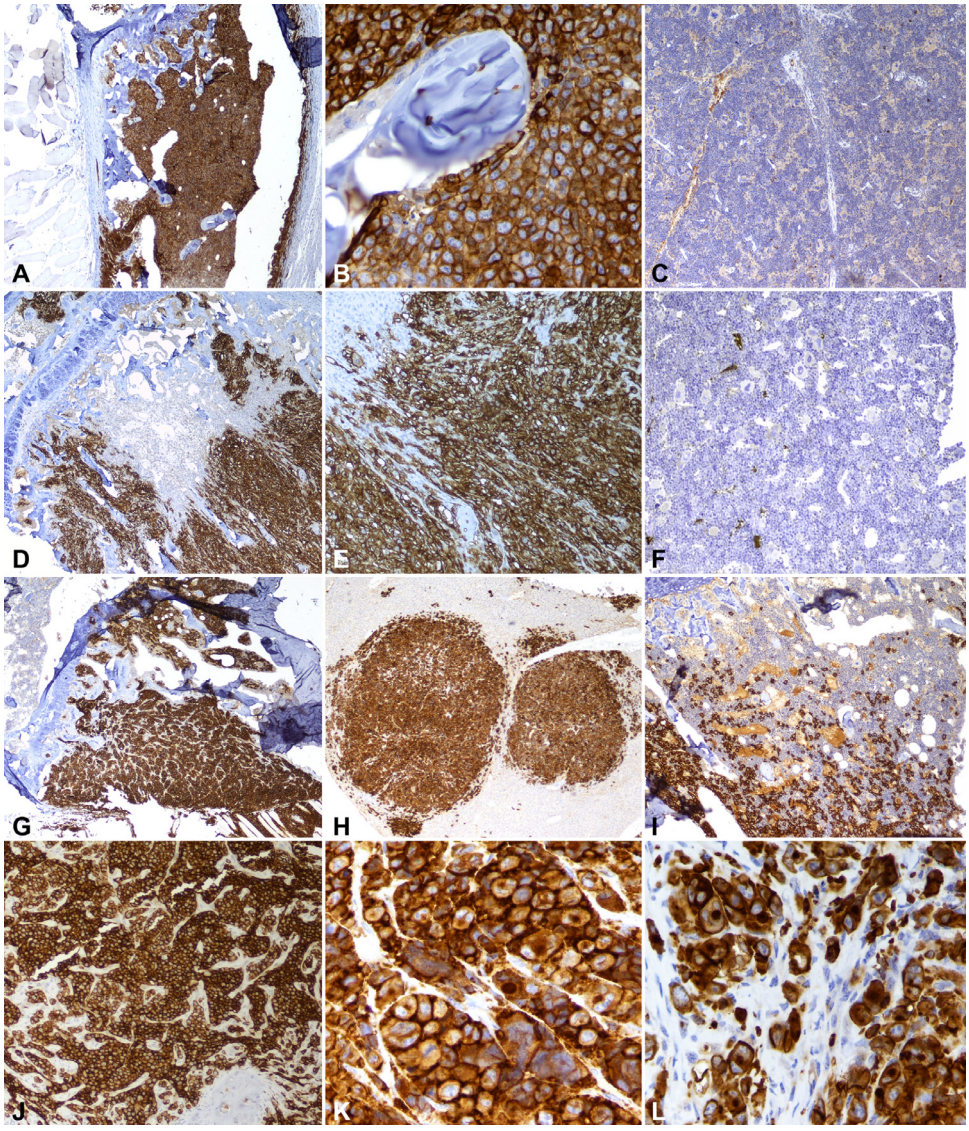

Fig. 2. Immunohistochemistry for human leukocyte antigen in ATL cells of a xenograft tibial tumor. ATL and Jurkat intratibial tumors were confirmed to be of human origin by staining for HLA: (A) Jurkat cells (magnification = 40X), (B) Jurkat (200X), (C) Jurkat (spleen, negative control, 100X), (D) HT1-RV cells (40X), (E) HT1-RV (100X), (F) HT1-RV (spleen, 100X), (G) RV-ATL cells (40X), (H) ATL-ED cells (40X), (I) TL-Om1 cells (100X), (J) RV-ATL (100X), (K) ATL-ED (400X), (L) TL-Om1 (400X).

in the RV-ATL tumors were increased compared to Jurkat tumors (Fig. 8(A)–(D)). Cytologic evaluation of the RV-ATL cells revealed an atypical round cell population with a high nuclear to cytoplasmic ratio. The TL-Om1 cell line had regional invasion into the metaphysis and diaphysis and also into the adjacent soft tissues surrounding the metaphysis through the 'cut back' zone of the cortex (Fig. 7(D)). Osteoclasts, osteoblasts, and bone-lining cells were quiescent. Impression smears of TL-Om1 tumors revealed a moderately atypical round cell population characterized by a high nuclear to cytoplasmic ratio.

Jurkat tumors proliferated within the medullary cavity of the tibias and elicited minimal bone cell response. An atypical round cell

Table 2
In vivo characteristics and bone pathology of ATL models.

Cell line	Origin	Tax mRNA level	Hbz mRNA level	Osteolysis	Osteosclerosis	New bone	Femur INV	Skeletal Muscle INV	Metastasis
RV-ATL	L	–	+	Marked	Mild	Mild	+/−	+	–
HT-1RV	L + IT	+ + +	+ +	Moderate	Moderate	Moderate	+/−	+	+
ATL-ED	L	–	+	Mild	Marked	Marked	+/−	+	+
TL-Om1	L	–	+	Mild	Mild	Mild	−	+	–
Jurkat	L	–	–	Mild	Mild	Mild	+	–	–

Tax and Hbz mRNA expression was measured by qRT-PCR (Fig. 10, + + + Crossing point (Cp) < 20, + + Cp = 20–25, + Cp = 25–30, − Cp > 30). The degree of osteolysis was determined by calculating the percentage of bone loss on radiographs (Fig. 5, Mild = 2.5–7.5% bone loss; Moderate = 7.5–15%; Marked > 15%). Intramedullary osteosclerosis, periosteal new bone formation, adjacent femur and skeletal muscle invasion, and distant metastasis were evaluated by histopathology, radiography and μCT imaging. *L, leukemic; IT, *in vitro* transformed; −, negative; +, positive; +/−, inconsistent but observed; INV, invasion.

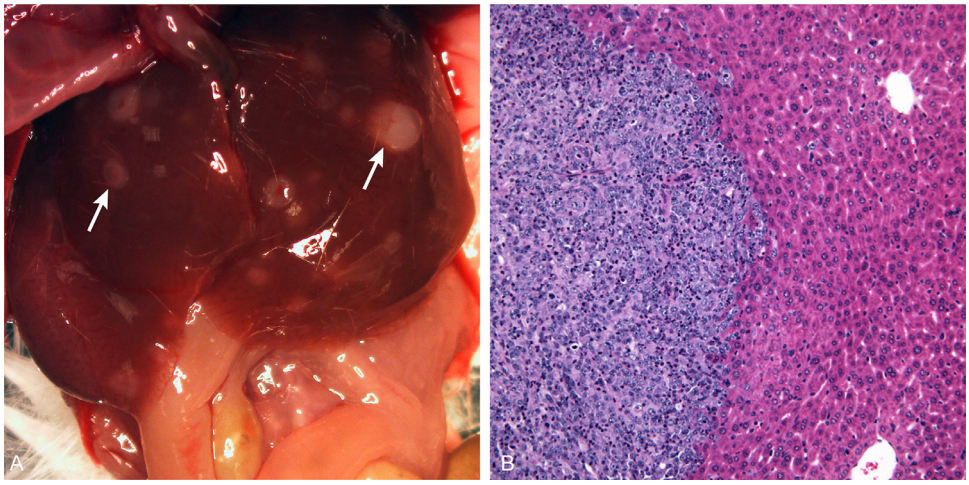

Fig. 3. Liver metastasis of ATL-ED intratibial xenograft. (A) There were metastases (white arrows) in the liver following intratibial injection of ATL-ED cells. (B) H&E-stained slide of a liver micrometastasis (magnification = 200X).

population diffusely expanded and replaced normal marrow constituents (Fig. 7(E)) with regions of marrow necrosis. Despite the numerous Jurkat cells within the bone, the cortices remained intact. Occasional spicules of woven bone were seen extended into the center of the marrow. The atypical tumor cells were present adjacent to the preexisting trabeculae and coexisted with quiescent bone-lining cells, OCs, and OBs (lower panel).

3.5. Bioluminescent imaging of ATL bone metastasis revealed visceral and bone tumor growth

To monitor tumor progression and metastatsis, the ATL-ED cell line was transduced with a firefly luciferase reporter. Bioluminescent imaging was performed on the day of injection and was used to confirm successful intratibial injections (Fig. 9(A)). Weekly imaging revealed an increase in tumor growth and metastasis (Fig. 9(B)). Tibial tumor growth rate was determined by measuring the average total flux (photons/s) per tibia over the course of 24 days. There was an 84-fold increase in ATL-ED-luc viable cell number from injection to the day of sacrifice as determined by the change in total flux (Fig. 9(C)). Distant metastases were observed in the liver (Fig. 3) and lung (Fig. 9(B)). Therefore, the ATL-ED model can be used to investigate tumor-bone interactions in the marrow, and distant metastases.

3.6. ATL xenograft phenotypic diversity was mirrored by diversity in mRNA expression of tumor-related bone factors

Radiography and histopathology showed significant differences in tumor-bone phenotypes in ATL xenograft mice. To investigate potential mechanisms and signaling pathways involved, we measured several pro- and anti-osteolytic tumor-associated mRNAs along with Tax and Hbz in the ATL cell line xenografts using qRT-PCR and human-specific primers (Fig. 10 and Table 1). RANKL is a key factor for the activation of osteoclast differentiation and activation and its synthesis is triggered by PTHRP stimulation of osteoblasts [34]. Osteoprotegerin (OPG) is known as a decoy receptor for RANKL. LPAR1, TNF, CCL3, and CSF1 are factors also known to have a role in osteoclast differentiation and activation in bone-tropic tumors. As expected, Tax mRNA was undetectable in all of our xenografts except HT-1RV, where it was expressed at high levels, while Hbz mRNA expression was moderate in the ATL bone tumors, but >15-fold greater in the HT-1RV bone tumors. HBZ expression was 1.5–3.1-fold higher in the bone tumors compared to the original uninjected cell lines, while Tax expression was increased ~2-fold in the HT1RV bone tumors (data not shown). With regard to

Fig. 4. Radiographs of ATL and Jurkat tibial xenograft tumors. (A) ATL-ED tumors demonstrated increased radiopacity (osteosclerosis) within the proximal tibia and metaphysis, in addition, new bone was present along the caudal periosteum. (B) HT-1RV bone tumors had increased radiopacity within the proximal tibia with multifocal punctate radiolucent foci. (C) RV-ATL tumors demonstrated large focal, radiolucent areas within the proximal tibia consistent with bone loss. (D) TL-Om1 bone tumors revealed increased intramedullary radiopacity with smooth, intact cortical surfaces. (E) Jurkat tumors demonstrated minimal radiographic changes.

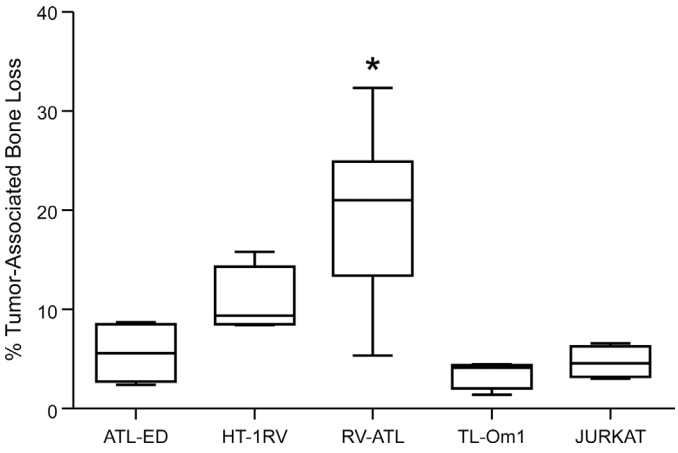

Fig. 5. Bone loss for ATL and Jurkat xenograft tibial tumors. The degree of radiolucency was quantified on the radiographs of tumor-bearing tibias as described in Methods. Jurkat, HT1-RV and TL-Om1 (n = 4 tibias each), ATL-ED (n = 5 tibias), RV-ATL (n = 6 tibias). The '*' symbol represents a p value of less than 0.05 as determined by one-way ANOVA. Tibias with RV-ATL tumors had significantly greater bone loss per total bone volume when compared to other ATL and Jurkat tumors.

the bone factors, RV-ATL xenografts expressed the highest of amount of PTHRP, RANKL, and OPG mRNA. HT-1RV xenografts expressed the highest of amount of parathyroid hormone/PTHRP receptor 1 (PTH1R), CCL3 (MIP-1α), OPG, CSF1 and TNF mRNA. TL-Om1 xenografts expressed the highest of amount of LPAR1 mRNA. The differences in mRNA expression between the different tumors was consistent with their phenotypic diversity and sheds light into potential mechanisms and signaling pathways involved.

4. Discussion

Several mouse models exist to study the pathogenesis of HTLV-1 and ATL. Transgenic mice with HTLV-1-specific protein expression have provided insight into the specific roles that Hbz and Tax play in the development of leukemia/lymphoma, and HTLV-1-infected humanized mice have been useful to investigate host responses in ATL and testing of novel therapeutics [35–37]. While xenograft mouse models of ATL have been used to investigate ATL tumor cell progression, invasion, interaction with the microenvironment and paraneoplastic syndromes [27,38], the availability of *in vivo* models to investigate ATL bone interactions is limited. Given the significant impact that bone involvement has on patient morbidity and resistance to chemotherapy, it would be invaluable to have a reproducible animal model to elucidate the tumor-bone interactions and investigate novel therapies for ATL in bone. In this study, we established and characterized a novel mouse model of ATL in bone. Due to the difficulty in assessing tumor burden and progression *in vivo*, we successfully transduced an ATL cell line that consistently results in pathologic tumor-induced bone changes with a lentivirus containing the luciferase gene to allow for noninvasive tumor detection and monitoring using bioluminescence.

The SCID mouse was developed in 1983 and was commonly used for the transplantation of human cancer cells. These mice do not have functional B or T cells, but do have residual natural killer (NK) cell activity [39]. Refinement of this model resulted in the development of the NOD/SCID mouse that has reduced NK cell activity [40–42]. Xenograft studies in ATL have largely employed the NOD/SCID model with a higher rate of ATL engraftment due to the reduced NK cell function and the resulting inability of NOD/SCID mice to recognize and eliminate Tax-expressing cells [19,40]. In recent years, xenograft success of human cancer cell lines was further advanced with the advent of the NSG mouse. These mice are based on the NOD/SCID background and have a deletion in the gamma chain of the interleukin 2 receptor.

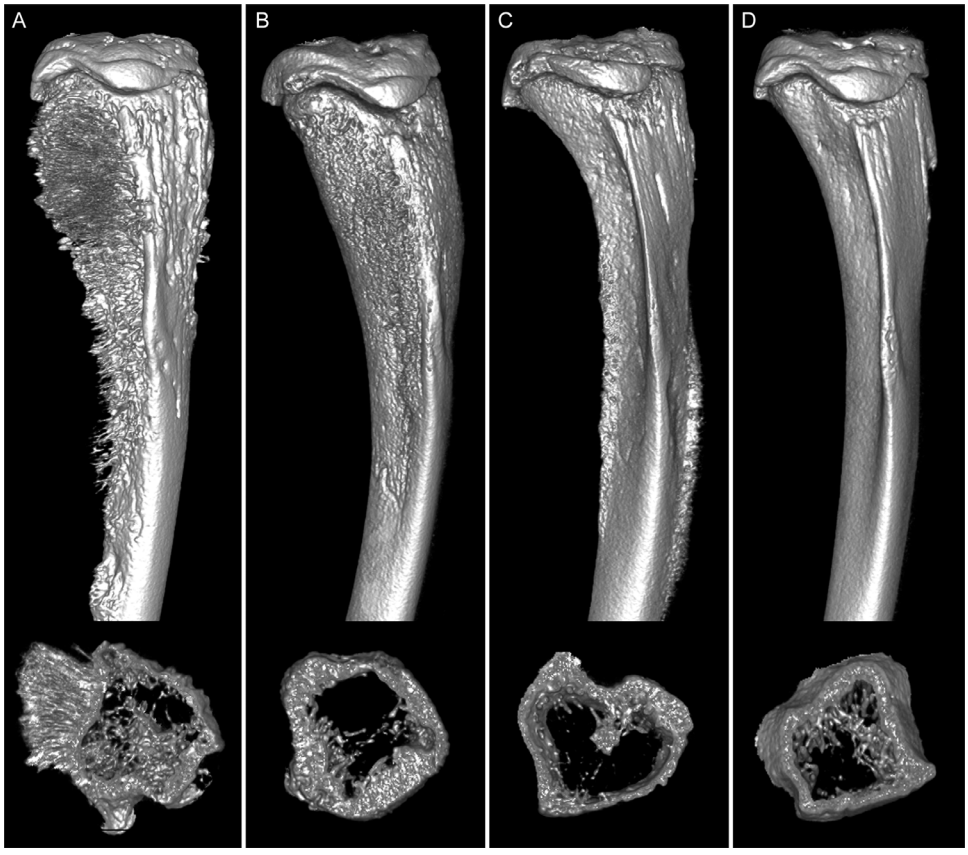

Fig. 6. μCT 3D reconstructions of ATL and Jurkat xenograft tibial tumors. Longitudinal and transverse sections of μCT 3D reconstructions of tibias with ATL and Jurkat bone tumors. (n = 2 for each cell line) (A) ATL-ED-bearing tibias had marked periosteal bone formation spanning the medial and lateral region of the tibia. Transverse sections demonstrated an increase in endosteal new bone (intramedullary osteosclerosis) (lower panel). (B) The HT-1RV-bearing tibias had an irregular periosteal surface from the proximal metaphysis to the distal diaphysis. Minimal amounts of medullary bone were present in tibias with HT-1RV tumors, indicative of intramedullary bone loss (lower panel). (C) Tibias from the TL-Om1-bearing mice had minimal changes in the tibias; however, they had decreased trabecular bone (lower panel). (D) Tibias with Jurkat tumors had smooth external cortical surfaces with minimal evidence of lysis or pathologic new bone formation. Transverse sections of tibias with Jurkat tumors had normal amounts of trabecular bone (lower panel).

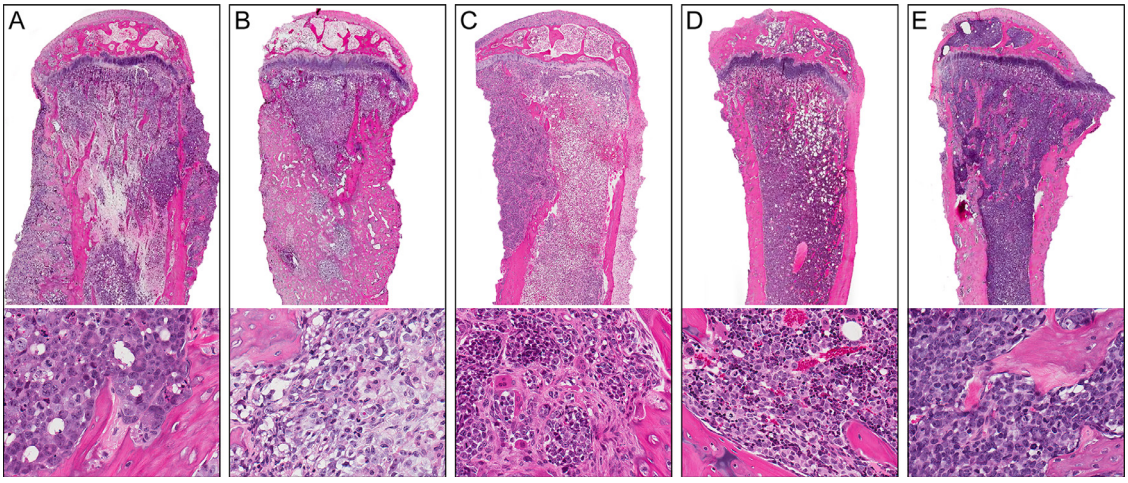

Fig. 7. Histopathology of ATL and Jurkat xenograft tibial tumors. Photomicrographs of H&E-stained tibias with ATL and Jurkat tumors. (A) ATL-ED bone tumors were characterized by invasion through and resorption of the cortex with marked periosteal new bone formation. Coagulation necrosis, fibrosis, and osteosclerosis were present throughout the medullary cavity with extensive tumor-induced new bone formation (lower panel). (B) New woven bone formation was present in HT-1RV bone tumors extending from preexisting cortices into the medullary cavity. Reactive stromal cells were present and associated with the HT-1RV tumor cells (lower panel). (C) Marked osteoclastic bone resorption was present in RV-ATL tumors characterized by extensive erosion of cortical and trabecular surfaces. Hypertrophic osteoclasts were present admixed with tumor and stromal cells within the medullary cavity (lower panel). (D) Tibias of mice with TL-Om1 tumors had minimal bone response. Despite the replacement of normal marrow constituents with tumor, minimal activation of osteoblasts and osteoclasts were observed on trabeculae (lower panel). (E) Jurkat cells proliferated within the bone marrow and induced minimal bone cell response. Top panels (magnification = 20X), lower panels (400X).

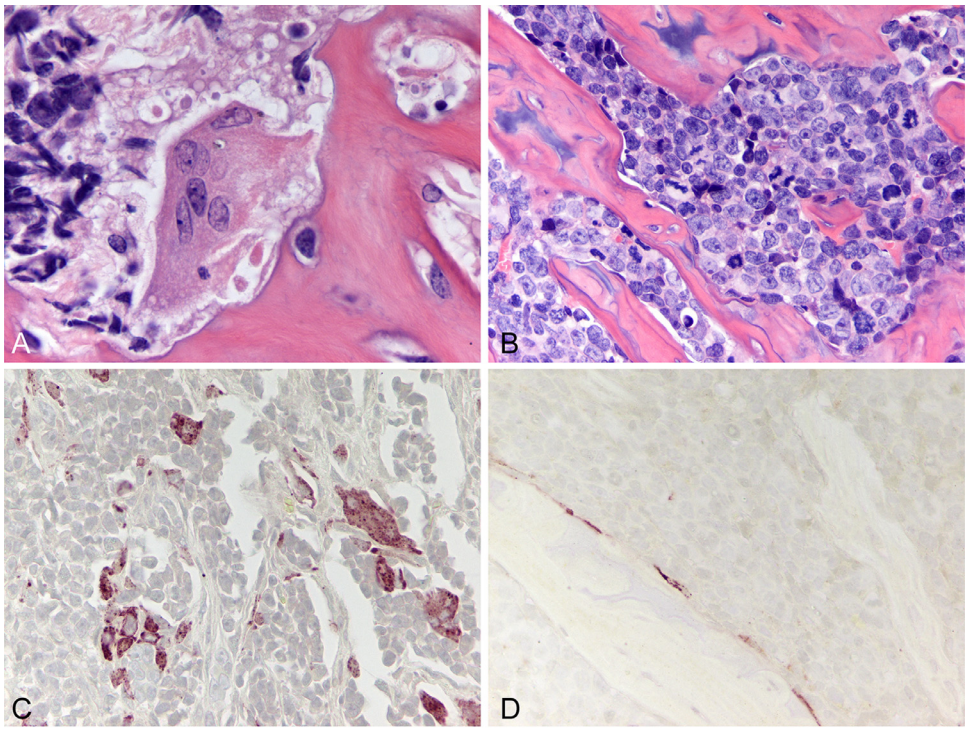

Fig. 8. H&E and TRAP-stained images of osteoclast activity in RV-ATL and Jurkat xenograft bone tumors. (A) There were markedly hypertrophic osteoclasts lining trabecular bone in an NSG mouse with an intratibial RV-ATL tumor. (magnification = 800X) (B) In contrast, osteoclasts in NSG mice with Jurkat tumors appeared normal with minimal activation. (400X) (C) TRAP staining displayed increased numbers of positively-stained hypertrophic multinucleate osteoclasts lining the resorbed bone surfaces in RV-ATL tumors. Osteoclasts were also found surrounded by tumor cells. (400X) (D) Positive TRAP staining of inactive osteoclasts in Jurkat tumors were present on the surfaces of trabecular bone. (200X).

This leads to a defect in the ability of dendritic cells to secrete interferon-gamma (IFN-γ) when activated, causing a near complete ablation of both innate and adaptive immunity that allows efficient human tumor engraftment [43–45].We evaluated engraftment potential of ATL cells in bone in the NOD/SCID and NSG strains. While tumor development was observed with the TL-Om1 and RV-ATL intratibial injections in the NOD/SCID mice, the HT-1RV cell line, which expresses high levels of Tax, failed to engraft in the NOD/SCID mice. This is consistent with previous reports suggesting that Tax serves as a potent stimulus of the immune response. All ATL lines, including HT1-RV, showed improved engraftment in the more highly immunodeficient NSG strain.

While paraneoplastic bone loss is common in ATL patients, primary ATL bone tumors resulting in local solitary or multiple lytic lesions also have been described [14,27,46–49]. While the role of the endocrine factors that mediate HHM and widespread bone resorption in ATL have been investigated, the description of the direct interaction between ATL and the cells of the bone microenvironment has largely been limited to case reports. Bone lesions are observed in 5.5% of ATL patients, mainly in the tibia, ulna, scapula, femur, clavicle, and peripheral extremities [14,49,50]. Regardless of the presence or absence of tumor cells, bone biopsies of ATL patients consistently demonstrate a marked increase in number and activation of osteoclasts lining the bone trabeculae and

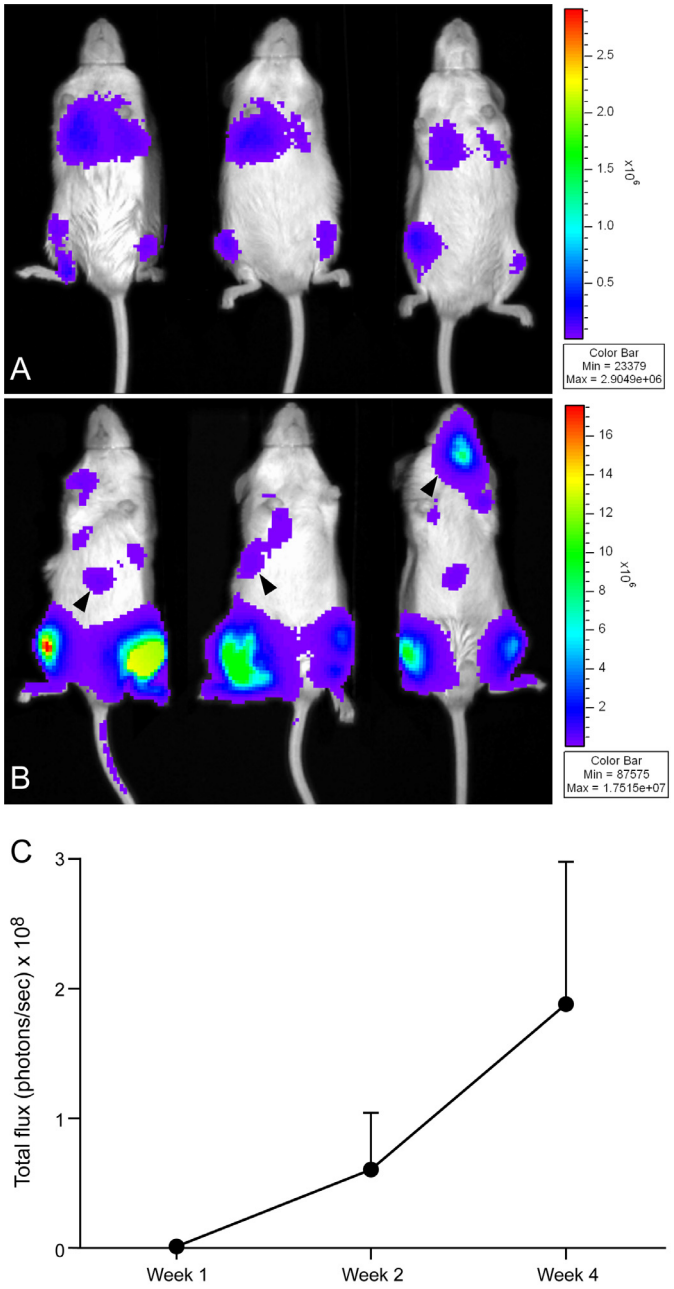

Fig. 9. *In vivo* bioluminescent imaging of tumor growth and progression of the ATL-ED intratibial xenograft model. The highest level of photon emission corresponded to the red end of the color spectrum. (A) Bioluminescent imaging performed on the day of injection confirmed correct intratibial injections as noted by photon signals in both left and right tibias and in the lungs (indicative of tumor cells in the vasculature). (B) Fourteen days following injection photon intensity was increased, correlating with progressive growth of ATL-ED tumors. In addition, some of the mice displayed distant metastases (black arrowheads) (C) The photon emission of each tibia of ATL-ED-luc mice was identified as the region of interest. Total flux (photons/s) was calculated for each region of interest and averaged. There was an 84-fold increase in ATL-ED-luc tumor growth at 24 days following injection. Week 1 (n = 14 tibias), week 2 (n = 12), week 4 (n = 6).

cortices, resulting in either local or systemic bone loss [1]. Osteoblast activation and extensive fibrosis have also been described [1,51,52]. Osteoporosis, pathologic fractures, and primary confinement to the marrow also have been observed in ATL patients, indicative of heterogeneity in the disease and its interaction with bone [15,16,53–55]. Our research using xenograft models of ATL interactions reproduces the diversity of bone phenotypes observed in ATL patients. ATL-ED has a predominantly osteoblastic pattern, with relatively little osteolysis, and conversely RV-ATL is primarily osteolytic, while HT-1RV has a mixed osteolytic/osteoblastic pattern. TL-Om1 shows diffuse marrow involvement after implantation, but causes little change in bone structure.

To investigate potential factors and signaling pathways responsible for the variety of bone phenotypes, qRT-PCR was performed on several bone signaling mRNAs in ATL xenograft tumors. PTHrP stimulates the shared parathyroid hormone/PTHRP receptor 1 (PTH1R), which is found on osteoblasts, osteocytes, and their precursors. The effects of PTH1R stimulation are context-dependent, and can result in the secretion of factors that activate OCs and cause bone resorption [56–58], as well as stimulating direct bone formation (add ref for anabolic role). PTHRP is highly expressed in ATL patients with both hypercalcemia and normocalcemia. Although the most osteolytic cell line, RV-ATL, expressed the highest levels of PTHrP, this factor was also increased in TL-Om1, which did not show osteolysis, and all of our models were normocalcemic. The lack of elevation in serum calcium may be due to the focal nature of bone involvement in this direct inoculation protocol. A potential autocrine role for PTHRP in HTLV-I transformation has also been described [59,60]. HT-1RV was the only model that showed high expression of PTH1R, as well as some PTHrP, which could allow autocrine signaling. Since the expression of PTHrP alone does not directly correlate with the ATL effects on bone, it is likely other tumor-derived factors are also important.

We analyzed the expression of several bone signaling mRNAs by qRT-PCR (Fig. 10). Each of the cell lines had a different pattern of expression of these mRNAs. The variation in tumor expression of bone-acting factors suggests that there is no single mediator of ATL effects on bone, and this panel of models could be useful to delineate the range of factors potentially involved. The ATL cell line with the greatest extent of osteolytic bone resorption and destruction was the RV-ATL tibial xenograft, which also had the highest expression of PTHrP and RANKL mRNA. RV-ATL cells also had increased expression of OPG compared to ATL-ED and TL-Om1, but this amount paled in comparison to the amount of RANKL that was expressed and, thus, it is unlikely to play a significant role in the RV-ATL bone phenotype.

HT-1RV cells were derived from RV-ATL cells by superinfection with HTLV-1. Tax is silenced (5′ deletion, hypermethylation, mutation) in the majority of ATL patients, while Hbz is expressed in most ATL patients. HT-1RV expressed very high levels of Tax mRNA (similar to GAPDH mRNA levels), whereas the other three cell lines expressed essentially undetectable amounts of Tax mRNA. Hbz mRNA was already expressed at moderate levels in the ATL cell lines, but it was increased an additional 24-fold in HT-1RV cells. In addition, PTHRP and RANKL were significantly downregulated (10- and 140-fold, respectively) in HT-1RV compared to RV-ATL xenografts, with no change in the amount of OPG mRNA. It is possible that PTHRP and RANKL were primarily responsible for the high level of bone loss in RV-ATL xenografts, compared to the moderate bone loss that in HT-1RV xenografts. However, several osteolytic factors were higher in HT-1RV [CCL3 (7-fold), CSF1 (25-fold) and/or TNF (770-fold)] again indicating that simply evaluating particular factors is unlikely to reflect the complex biology of the bone microenvironment and its response to tumors.

Tumors derived from TL-Om1 cells, which caused little change in the bone, also showed low expression of osteolytic factors, except for LPAR1. ATL-ED tumors were the most osteosclerotic of the tumors and had a low amount of bone loss. Therefore, it was not surprising that ATL-ED tumors expressed the lowest amount of each of the osteolytic mRNAs that were examined. Further work is required to define the factors/pathways that are involved in the increased periosteal new bone and intramedullary osteosclerosis of ATL-ED xenografts.

In conclusion, we report the generation and characterization of a novel ATL bone tumor model. The variation in tumor-bone phenotypes observed with the different cell lines illustrates the complexity of

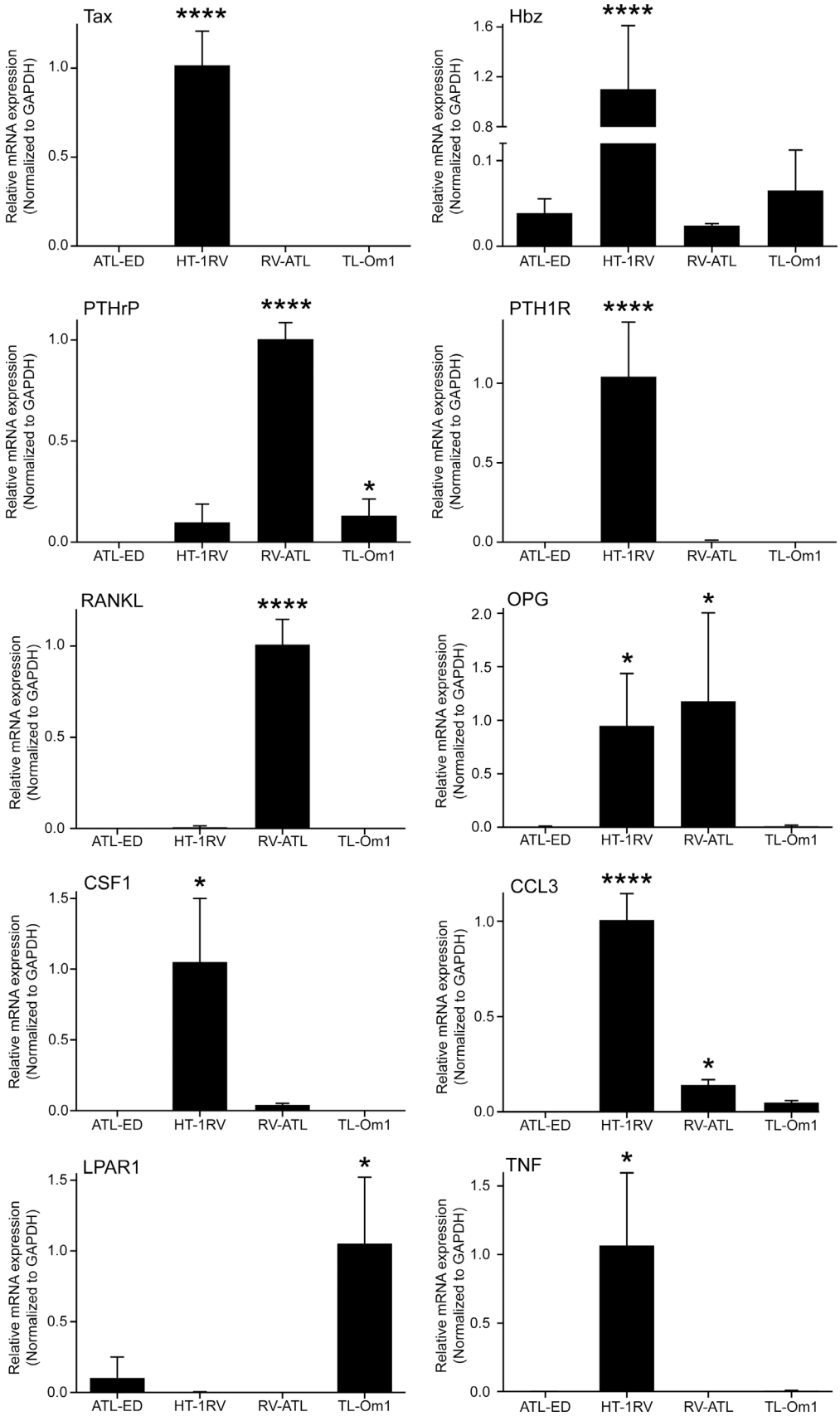

Fig. 10. qRT-PCR of viral and bone-signaling mRNAs in ATL xenograft bone tumors. To investigate signaling pathways and factors responsible for the variation in tumor-bone phenotypes, qRT-PCR was performed on several bone signaling mRNAs in ATL xenograft tumors. The variation in tumor expression of bone-acting factors reflected the heterogeneity observed in the tumor-bone phenotypes of ATL intratibial xenograft mice. Since ATL-ED xenografts expressed the lowest amounts of most of the mRNAs examined, all the other cell lines were compared against ATL-ED. RV-ATL ($n = 3$ tumor samples), HT1-RV ($n = 4$), ATL-ED ($n = 5$), TL-Om1 ($n = 6$). A one-way ANOVA test was used for statistical comparison and the '*' symbol indicates a $p < 0.05$; '**' symbol indicates a $p < 0.01$; '***' symbol indicates a $p < 0.001$; '****' symbol indicates a $p < 0.0001$.

tumor-bone pathobiology. For example, if an investigator wants to study the osteoblastic component of ATL, the ATL-ED cells will be the best choice. If they would like to study osteolysis in ATL, they should choose the RV-ATL cells, which are very osteolytic. The HT1-RV and TL-Om1 cells represent an intermediate phenotype with or without Tax expression, respectively. Therefore, these mouse models recapitulate key interactions between ATL and bone and will be useful for investigations on the interactions and mechanisms responsible for ATL bone metastasis.

Declaration of Competing Interest

None.

Acknowledgments

This work was funded through grants from the National Cancer Institute (P01 CA100730 to TJR, KNW and PLG) and (T32 OD010429 to NAK). Animal research reported in this publication was supported by the Ohio State University Comprehensive Cancer Center and the National Institutes of Health under grant number P30 CA016058. We thank the Target Validation Shared Resource (TVSR) at the Ohio State University Comprehensive Cancer Center for providing the NSG mice used in the preclinical studies described herein. The content is solely the responsibility of the authors and does not necessarily represent the official views of the National Institute of Health. We thank Alan Flechtner and Anne Saulsbery for tissue processing and preparation of slides. We thank Lianbo Yu form the OSU Center for Biostatistics and Bioinformatics for his assistance with some of the statistics. Finally, we thank our medical illustrator Tim Vojt for his invaluable assistance in creating all the figures.

References

[1] J. Haratake, A. Horie, S. Oda, S. Chiba, K. Kobori, H. Sato, A clinicopathological review of 12 autopsied cases of adult T-cell leukemia, Acta Pathol. Jpn. 36 (3) (1986) 349–362.
[2] K. Kato, K. Akashi, Recent advances in therapeutic approaches for adult T-cell leukemia/lymphoma, Viruses 7 (12) (2015) 6604–6612.
[3] R.L. Graham, M. Burch, J.R. Krause, Adult T-cell leukemia/lymphoma, Proc. (Bayl. Univ. Med. Cent.) 27 (3) (2014) 235–238.
[4] H. Katsuya, K. Ishitsuka, A. Utsunomiya, S. Hanada, T. Eto, Y. Moriuchi, Y. Saburi, M. Miyahara, E. Sueoka, N. Uike, S. Yoshida, K. Yamashita, K. Tsukasaki, H. Suzushima, Y. Ohno, H. Matsuoka, T. Jo, M. Amano, R. Hino, M. Shimokawa, K. Kawai, J. Suzumiya, K. TamuraA.T.-P.I. Project, Treatment and survival among 1594 patients with ATL, Blood 126 (24) (2015) 2570–2577.
[5] D. Prager, J.D. Rosenblatt, E. Ejima, Hypercalcemia, parathyroid hormone-related protein expression and human T-cell leukemia virus infection, Leuk. Lymphoma 14 (5–6) (1994) 395–400.
[6] L. Ratner, Adult T cell leukemia lymphoma, Front. Biosci. 9 (2004) 2852–2859.
[7] M. Shimoyama, Diagnostic criteria and classification of clinical subtypes of adult T-cell leukaemia-lymphoma. A report from the lymphoma study group (1984–87), Br. J. Haematol. 79 (3) (1991) 428–437.
[8] S.T. Shu, C.K. Martin, N.K. Thudi, W.P. Dirksen, T.J. Rosol, Osteolytic bone resorption in adult T-cell leukemia/lymphoma, Leuk. Lymphoma 51 (4) (2010) 702–714.
[9] C.Z. Giam, O.J. Semmes, HTLV-1 infection and adult T-cell leukemia/lymphoma – a tale of two proteins: tax and HBZ, Viruses 8 (6) (2016).
[10] K. Nosaka, T. Miyamoto, T. Sakai, H. Mitsuya, T. Suda, M. Matsuoka, Mechanism of hypercalcemia in adult T-cell leukemia: overexpression of receptor activator of nuclear factor kappaB ligand on adult T-cell leukemia cells, Blood 99 (2) (2002) 634–640.
[11] Y. Okada, J. Tsukada, K. Nakano, S. Tonai, S. Mine, Y. Tanaka, Macrophage inflammatory protein-1alpha induces hypercalcemia in adult T-cell leukemia, J. Bone Miner. Res. 19 (7) (2004) 1105–1111.
[12] S.T. Shu, M.V. Nadella, W.P. Dirksen, S.A. Fernandez, N.K. Thudi, J.L. Werbeck, M.D. Lairmore, T.J. Rosol, A novel bioluminescent mouse model and effective therapy for adult T-cell leukemia/lymphoma, Cancer Res. 67 (24) (2007) 11859–11866.
[13] K. Yamaguchi, T. Kiyokawa, T. Watanabe, T. Ideta, K. Asayama, M. Mochizuki, A. Blank, K. Takatsuki, Increased serum levels of C-terminal parathyroid hormone-related protein in different diseases associated with HTLV-1 infection, Leukemia 8 (10) (1994) 1708–1711.
[14] S. Ehara, K. Takahashi, J. Nishida, M. Uetani, K. Ohashi, T. Aoki, Hand osteolysis in patients with adult T-cell leukemia-lymphoma: radiographic characteristics, Tohoku J. Exp. Med. 236 (1) (2015) 63–69.
[15] T. Hara, S. Wakatsuki, S. Ozaki, M. Abe, M. Kosaka, Primary adult T-cell leukemia/lymphoma of bone, Int. J. Hematol. 79 (2) (2004) 157–160.
[16] T. Ohuchida, H. Nishitani, N. Kamikawaji, Y. Niho, T. Ooiwa, K. Matsuura, "Adult T-cell leukemia/lymphoma" with bone demineralization, Skeletal. Radiol. 14 (3) (1985) 194–197.
[17] K.N. Weilbaecher, T.A. Guise, L.K. McCauley, Cancer to bone: a fatal attraction, Nat. Rev. Cancer 11 (6) (2011) 411–425.
[18] Y. Zheng, H. Zhou, C.R. Dunstan, R.L. Sutherland, M.J. Seibel, The role of the bone microenvironment in skeletal metastasis, J. Bone Oncol. 2 (1) (2013) 47–57.
[19] G. Feuer, S.A. Stewart, S.M. Baird, F. Lee, R. Feuer, I.S. Chen, Potential role of natural killer cells in controlling tumorigenesis by human T-cell leukemia viruses, J. Virol. 69 (2) (1995) 1328–1333.
[20] G. Feuer, J.A. Zack, W.J. Harrington Jr., R. Valderama, J.D. Rosenblatt, W. Wachsman, S.M. Baird, I.S. Chen, Establishment of human T-cell leukemia virus type i T-cell lymphomas in severe combined immunodeficient mice, Blood 82 (3) (1993) 722–731.
[21] A.R. Panfil, J. Al-Saleem, C.M. Howard, J.M. Mates, J.J. Kwiek, R.A. Baiocchi, P.L. Green, PRMT5 is upregulated in HTLV-1-mediated T-cell transformation and selective inhibition alters viral gene expression and infected cell survival, Viruses 8 (1) (2015).
[22] S. Takeda, M. Maeda, S. Morikawa, Y. Taniguchi, J. Yasunaga, K. Nosaka, Y. Tanaka, M. Matsuoka, Genetic and epigenetic inactivation of tax gene in adult T-cell leukemia cells, Int. J. Cancer 109 (4) (2004) 559–567.
[23] K. Sugamura, M. Fujii, M. Kannagi, M. Sakitani, M. Takeuchi, Y. Hinuma, Cell surface phenotypes and expression of viral antigens of various human cell lines carrying human T-cell leukemia virus, Int. J. Cancer 34 (2) (1984) 221–228.
[24] S.A. Stewart, G. Feuer, A. Jewett, F.V. Lee, B. Bonavida, I.S. Chen, HTLV-1 gene expression in adult T-cell leukemia cells elicits an NK cell response *in vitro* and correlates with cell rejection in SCID mice, Virology 226 (2) (1996) 167–175.
[25] M.V. Nadella, W.P. Dirksen, K.S. Nadella, S. Shu, A.S. Cheng, J.A. Morgenstern, V. Richard, S.A. Fernandez, T.H. Huang, D. Guttridge, T.J. Rosol, Transcriptional regulation of parathyroid hormone-related protein promoter P2 by NF-KAPPAB in adult T-cell leukemia/lymphoma, Leukemia 21 (8) (2007) 1752–1762.
[26] J.K. Simmons, W.P. Dirksen, B.E. Hildreth 3rd, C. Dorr, C. Williams, R. Thomas, M. Breen, R.E. Toribio, T.J. Rosol, Canine prostate cancer cell line (Probasco) produces osteoblastic metastases *in vivo*, Prostate 74 (13) (2014) 1251–1265.
[27] V. Richard, M.D. Lairmore, P.L. Green, G. Feuer, R.S. Erbe, B. Albrecht, C. D'Souza, E.T. Keller, J. Dai, T.J. Rosol, Humoral hypercalcemia of malignancy: severe combined immunodeficient/beige mouse model of adult T-cell lymphoma independent of human T-cell lymphotropic virus type-1 tax expression, Am. J. Pathol. 158 (6) (2001) 2219–2228.
[28] K.M. Kodigepalli, M. Li, S. Bonifati, A.R. Panfil, P.L. Green, S.L. Liu, L. Wu, SAMHD1 inhibits epithelial cell transformation *in vitro* and affects leukemia development in xenograft mice, Cell Cycle 17 (23) (2018) 2564–2576.
[29] V. Richard, A. Luchin, R.M. Brena, C. Plass, T.J. Rosol, Quantitative evaluation of alternative promoter usage and 3′ splice variants for parathyroid hormone-related protein by real-time reverse transcription-PCR, Clin. Chem. 49 (8) (2003) 1398–1402.
[30] S.M. Elshafae, N.A. Kohart, L.A. Altstadt, W.P. Dirksen, T.J. Rosol, The effect of a histone deacetylase inhibitor (AR-42) on canine prostate cancer growth and metastasis, Prostate 77 (7) (2017) 776–793.
[31] L.D. Shultz, B.L. Lyons, L.M. Burzenski, B. Gott, X. Chen, S. Chaleff, M. Kotb, S.D. Gillies, M. King, J. Mangada, D.L. Greiner, R. Handgretinger, Human lymphoid and myeloid cell development in NOD/LtSz-scid IL2R gamma null mice engrafted with mobilized human hemopoietic stem cells, J. Immunol. 174 (10) (2005) 6477–6489.
[32] J. Schueler, D. Wider, K. Klingner, G.M. Siegers, A.M. May, R. Wasch, H.H. Fiebig, M. Engelhardt, Intratibial injection of human multiple myeloma cells in NOD/SCID IL-2Rgamma(null) mice mimics human myeloma and serves as a valuable tool for the development of anticancer strategies, PLoS ONE 8 (11) (2013) e79939.
[33] G.P. Taylor, M. Matsuoka, Natural history of adult T-cell leukemia/lymphoma and approaches to therapy, Oncogene 24 (39) (2005) 6047–6057.
[34] T.J. Martin, Osteoblast-derived PTHRP is a physiological regulator of bone formation, J. Clin. Investig. 115 (9) (2005) 2322–2324.
[35] L. Gao, H. Deng, H. Zhao, A. Hirbe, J. Harding, L. Ratner, K. Weilbaecher, HTLV-1 tax transgenic mice develop spontaneous osteolytic bone metastases prevented by osteoclast inhibition, Blood 106 (13) (2005) 4294–4302.
[36] Y. Satou, J. Yasunaga, T. Zhao, M. Yoshida, P. Miyazato, K. Takai, K. Shimizu, K. Ohshima, P.L. Green, N. Ohkura, T. Yamaguchi, M. Ono, S. Sakaguchi, M. Matsuoka, HTLV-1 bZIP factor induces T-cell lymphoma and systemic inflammation *in vivo*, PLoS Pathog. 7 (2) (2011) e1001274.
[37] J. Villaudy, M. Wencker, N. Gadot, N.A. Gillet, J.Y. Scoazec, L. Gazzolo, M.G. Manz, C.R. Bangham, M.D. Dodon, HTLV-1 propels thymic human T cell development in "human immune system" Rag2(-)/(-) gamma c(-)/(-) mice, PLoS Pathog. 7 (9) (2011) e1002231.
[38] S. Niewiesk, Animals models of human T cell leukemia virus type I leukemogenesis, ILAR J. 57 (1) (2016) 3–11.
[39] G.C. Bosma, R.P. Custer, M.J. Bosma, A severe combined immunodeficiency mutation in the mouse, Nature 301 (5900) (1983) 527–530.
[40] Y. Liu, K. Dole, J.R. Stanley, V. Richard, T.J. Rosol, L. Ratner, M. Lairmore, G. Feuer, Engraftment and tumorigenesis of HTLV-1 transformed T cell lines in SCID/bg and NOD/SCID mice, Leuk. Res. 26 (6) (2002) 561–567.
[41] C. Parrula, B. Zimmerman, P. Nadella, S. Shu, T. Rosol, S. Fernandez, M. Lairmore, S. Niewiesk, Expression of tumor invasion factors determines systemic engraftment and induction of humoral hypercalcemia in a mouse model of adult T-cell leukemia,

Vet. Pathol. 46 (5) (2009) 1003–1014.
[42] L.D. Shultz, P.A. Schweitzer, S.W. Christianson, B. Gott, I.B. Schweitzer, B. Tennent, S. McKenna, L. Mobraaten, T.V. Rajan, D.L. Greiner, et al., Multiple defects in innate and adaptive immunologic function in NOD/LtSz-scid mice, J. Immunol. 154 (1) (1995) 180–191.
[43] M.A. Lawson, J.M. Paton-Hough, H.R. Evans, R.E. Walker, W. Harris, D. Ratnabalan, J.A. Snowden, A.D. Chantry, NOD/SCID-GAMMA mice are an ideal strain to assess the efficacy of therapeutic agents used in the treatment of myeloma bone disease, PLoS ONE 10 (3) (2015) e0119546.
[44] D. Chadalavada, T.W. Adamson, J.C. Burnett, R.W. Chen, J.J. Rossi, Irradiated compared with nonirradiated NSG mice for the development of a human B-cell lymphoma model, Comput. Med. 64 (3) (2014) 179–185.
[45] M. Ito, H. Hiramatsu, K. Kobayashi, K. Suzue, M. Kawahata, K. Hioki, Y. Ueyama, Y. Koyanagi, K. Sugamura, K. Tsuji, T. Heike, T. Nakahata, NOD/SCID/gamma(c) (null) mouse: an excellent recipient mouse model for engraftment of human cells, Blood 100 (9) (2002) 3175–3182.
[46] K. Chiba, S. Hashino, K. Izumiyama, N. Toyoshima, S. Suzuki, M. Kurosawa, M. Asaka, Multiple osteolytic bone lesions with high serum levels of interleukin-6 and ccl chemokines in a patient with adult T cell leukemia, Int. J. Lab. Hematol. 31 (3) (2009) 368–371.
[47] T. Takahashi, H. Tsukuda, H. Itoh, H. Kimura, M. Yoshimoto, M. Tsujisaki, Primary and isolated adult T-cell leukemia/lymphoma of the bone marrow, Intern. Med. 50 (20) (2011) 2393–2396.
[48] J. Aoki, I. Yamamoto, M. Hino, K. Torizuka, T. Uchiyama, H. Uchino, Case report 429: adult T-cell leukemia (ATL), Skeletal. Radiol. 16 (5) (1987) 412–415.
[49] T. Matsushima, M. Yamamoto, K. Sakai, Multiple osteolysis of peripheral extremities in a patient with adult T cell leukemia/lymphoma, Intern. Med. 38 (10) (1999) 820–823.
[50] G.D. Roodman, Mechanisms of bone lesions in multiple myeloma and lymphoma, Cancer 80 (8 Suppl) (1997) 1557–1563.
[51] T. Kiyokawa, K. Yamaguchi, M. Takeya, K. Takahashi, T. Watanabe, T. Matsumoto, S.Y. Lee, K. Takatsuki, Hypercalcemia and osteoclast proliferation in adult T-cell leukemia, Cancer 59 (6) (1987) 1187–1191.
[52] S. Qayyum, J.K. Choi, Adult T-cell leukemia/lymphoma, Arch. Pathol. Lab. Med. 138 (2) (2014) 282–286.
[53] S. Anzai, S. Takayasu, S. Fujiwara, M. Tateyama, H. Taira, M. Takashita, Elevation of IL-6 in ATL patient with a pathological fracture, J. Dermatol. 29 (10) (2002) 644–647.
[54] T. Kuriyama, N. Kawano, K. Yamashita, I. Kikuchi, Two cases of primary adult T-cell leukemia/lymphoma of bone: case reports and a review of the literature, Int. J. Hematol. (2016).
[55] B.L. Pear, Skeletal manifestations of the lymphomas and leukemias, Semin. Roentgenol. 9 (3) (1974) 229–240.
[56] T. Akatsu, N. Takahashi, N. Udagawa, K. Imamura, A. Yamaguchi, K. Sato, N. Nagata, T. Suda, Role of prostaglandins in interleukin-1-induced bone resorption in mice *in vitro*, J. Bone Miner. Res. 6 (2) (1991) 183–189.
[57] Y. Wano, T. Hattori, M. Matsuoka, K. Takatsuki, A.O. Chua, U. Gubler, W.C. Greene, Interleukin 1 gene expression in adult T cell leukemia, J. Clin. Investig. 80 (3) (1987) 911–916.
[58] I. Yamamoto, M. Kawano, T. Sone, K. Iwato, H. Tanaka, H. Ishikawa, N. Kitamura, K. Lee, C. Shigeno, J. Konishi, et al., Production of interleukin 1 beta, a potent bone resorbing cytokine, by cultured human myeloma cells, Cancer Res. 49 (15) (1989) 4242–4246.
[59] A. Wake, Y. Tanaka, K. Nakatsuka, M. Misago, S. Oda, I. Morimoto, S. Eto, Calcium-dependent homotypic adhesion through leukocyte function-associated antigen-1/intracellular adhesion molecule-1 induces interleukin-1 and parathyroid hormone-related protein production on adult T-cell leukemia cells *in vitro*, Blood 86 (6) (1995) 2257–2267.
[60] M.V. Nadella, S.T. Shu, W.P. Dirksen, N.K. Thudi, K.S. Nadella, S.A. Fernandez, M.D. Lairmore, P.L. Green, T.J. Rosol, Expression of parathyroid hormone-related protein during immortalization of human peripheral blood mononuclear cells by HTLV-1: implications for transformation, Retrovirology 5 (2008) 46.